

3D SIMULATIONS OF VISCOUS DISSIPATION IN THE INTRACLUSTER MEDIUM

MATEUSZ RUSZKOWSKI¹JILA, Campus Box 440, University of Colorado at Boulder, CO 80309-0440;
mr@quixote.colorado.edu

MARCUS BRÜGGEN

International University Bremen, Campus Ring 1, 28759 Bremen, Germany;
m.brueggen@iu-bremen.de

AND

MITCHELL C. BEGELMAN²JILA, Campus Box 440, University of Colorado at Boulder, CO 80309-0440;
mitch@jila.colorado.edu
accepted for ApJ

ABSTRACT

We present three-dimensional simulations of viscous dissipation of AGN induced gas motions and waves in clusters of galaxies. These simulations are motivated by recent detections of ripples in the Perseus and Virgo clusters. Although the sound waves generated by buoyant bubbles decay with distance from the cluster center, we show that these waves can contribute substantially to offsetting the radiative cooling at distances significantly exceeding the bubble size. The energy flux of the waves declines more steeply with radius than the inverse-square law predicted by energy conservation, implying that dissipation plays an important role in tapping the wave energy. We show that such dispersing sound waves/weak shocks are detectable as ripples on unsharp-masked X-ray cluster maps, and point out that the interfaces between the intracluster medium and old bubbles are also clearly detectable in unsharp-masked X-ray maps. This opens up the possibility of detecting fossil bubbles that are difficult to detect in radio emission. This mode of heating is consistent with other observational constraints, such as the presence of cool rims around the bubbles and the absence of strong shocks. Thus, the mechanism offers a way of heating clusters in a spatially distributed and gentle fashion. We also discuss the energy transfer between the central AGN and the surrounding medium. In our numerical experiments, we find that roughly 65 per cent of the energy injected by the AGN is transferred to the intracluster medium and approximately 25 percent of the injected energy is dissipated by viscous effects and contributes to heating of the gas. The overall transfer of heat from the AGN to the gas is comparable to the radiative cooling losses. The simulations were performed with the FLASH adaptive mesh refinement code.

Subject headings: cooling flows — galaxies: active — waves — galaxies: clusters: general — methods: numerical — intergalactic medium

1. INTRODUCTION

The long-standing problem of cooling flow clusters of galaxies, in which the central cooling time is much shorter than the Hubble time, is how to prevent the intracluster medium (ICM) from collapsing catastrophically on a short timescale. The original idea for maintaining the overall cluster stability (Fabian 1994) was to postulate that a certain amount of gas decouples from the flow and does not contribute to the cooling of the remaining gas. This model would require up to $1000 M_{\odot} \text{ yr}^{-1}$ in mass deposition rates to guarantee cluster stability. This has been found to be inconsistent with recent *Chandra* (e.g., McNamara et al. 2000, Blanton et al. 2001) and *XMM-Newton* observations (e.g., Peterson et al. 2001, 2003; Tamura et al. 2001). *Chandra* observations reveal a number of clusters with X-ray cavities/bubbles created by the central active galactic nuclei (AGN). It has been suggested by many authors that AGN feedback may play a crucial role in self-regulating cooling flows (e.g. Churazov et al. 2001, Ruszkowski &

Begelman 2002, Brighenti & Mathews 2003). One of the main outstanding issues is how the AGN heating comes about in detail. In principle, strong shocks generated by AGN outbursts can dissipate in the ICM and heat the gas. However, imaging observations of cooling flow cores do not give evidence for this mode of heating. Recent *Chandra* observations of two well-known clusters, the Perseus cluster (Fabian et al. 2003a,b) and the Virgo cluster (Forman et al. 2004), suggest that dissipation of sound waves and weak shocks could be an important source of gas heating — an idea first proposed by Fabian et al. (2003a). Further support for the idea that viscosity may play an important role in the ICM comes from a recent study of density profiles in clusters (Hansen & Stadel 2003). Recently, a number of papers have described simulations of bubble-heated clusters (e.g., Churazov et al. 2001, Brüggen et al. 2002, Brüggen & Kaiser 2002, Brüggen 2003, Quilis et al. 2001). Numerical simulations of viscous dissipation of AGN energy in ICM were previously considered by Ruszkowski et al. (2004) (Paper I) and Reynolds et al. (2004).

¹ *Chandra* Fellow² also at Department of Astrophysical and Planetary Sciences, University of Colorado at Boulder

The main purpose of this paper is to extend our previous work on viscous heating of the ICM by waves to three dimensions. The results of a simulation of viscous dissipation in three dimensions could differ from our previous two-dimensional results given that the amplitudes of waves decrease faster with radius in three dimensions. This would directly affect the spatial distribution of the viscous dissipation rate. Apart from performing our simulations in three dimensions, we extend our previous analysis and that of Reynolds et al. (2004) to include aspects of heating that were previously neglected. First, we show that the conclusions drawn from our 2D simulations carry over to three dimensions. Second, our new results include (i) X-ray maps and unsharp-masked X-ray images, (ii) extend the discussion of spatial distribution of energy dissipation and overall heating rate, (iii) present details of the flow of heat between the bubbles and the intracluster medium and (iv) discuss the wave decay rates.

The outline of this paper is as follows. In the next section we describe the assumptions of the model. Section 3 presents and discusses our results, focusing on the spatial distribution of heating. In particular, we discuss the detectability of the ripples/sound waves, their decay rate with distance from the center/bubble surface, the energy transfer from the AGN to the kinetic and thermal energy of the ICM, and the fraction of the dissipated energy that heats the gas. The fourth section discusses the limitations of our model. The final section summarizes our findings.

2. ASSUMPTIONS OF THE MODEL

The initial conditions, details of energy injection, dissipation and radiative cooling assumed in our simulations are similar to those in Ruszkowski et al. (2003). Here we only summarize the differences from Paper I.

Calculations were done in three dimensions in Cartesian geometry using the PPM adaptive mesh refinement code FLASH (version 2.3). Starting from a single top-level block and using block sizes of 16^3 zones we allowed for 5 levels of refinement, giving an effective number of 256^3 zones. The size of the computational domain was $(200 \text{ kpc})^3$, which corresponds to an effective resolution of $\sim 0.8 \text{ kpc}$. As previously, we employed outflow boundary conditions on all boundaries.

When the source is active, each of the active regions has a constant luminosity of $L = 1.6 \times 10^{45} \text{ erg s}^{-1}$ and the rate at which mass is injected into the active region is $\dot{\rho}V = 2.8 \text{ M}_\odot \text{yr}^{-1}$. The energy injection is intermittent with a period of 3×10^7 years, within which the source is active for 0.5×10^7 years. Thus, since there are two active regions in the source, the time-averaged luminosity is $\sim 5.3 \times 10^{44} \text{ erg s}^{-1}$. The motivation behind a different choice of source parameters in the 3D case is as follows. In 2D the code takes the input density (g cm^{-3}) and luminosity density ($\text{erg cm}^{-3} \text{ s}^{-1}$) and interprets them as surface quantities. That is, the hydrodynamic equations are effectively integrated along one axis by multiplying these quantities by a unit length. As the size of the active regions are smaller than unity, the code effectively assigns a bigger volume to the active region when the simulation is performed in 2D. The source luminosity density that enters the energy equation is a constant equal to L/V_b , where L is the source luminosity and $V_b = (4/3)\pi r_b^3$ is the bubble volume (the

same formula is used in the code in 2D and 3D simulations). This means that in order to supply the same energy to the cluster in 3D as in a 2D simulation, one has to convert the 2D luminosity to the 3D (real) luminosity using an approximate prescription $L_{3d} \sim (3/4)(\text{unit length}/r_b)L_{2d}$. The size of the active region in the 3D case was $r_b = 3 \text{ kpc}$. As far as the mass injection is concerned, we used higher values for purely pragmatic reasons. Higher injection rates assure that the densities in the active regions are reduced to a lesser degree than they would have been if the injection rate had been lower. This means that the constraints on the Courant timestep are less severe and the simulations can be performed in a shorter time.

We use the standard Spitzer viscosity for an unmagnetized plasma (Braginskii 1958), for which $\mu = 7.1 \times 10^{-17}(\ln \Lambda/31)^{-1}T^{5/2} \text{ g cm}^{-1} \text{ s}^{-1}$. As conditions inside the buoyantly rising bubbles are very uncertain and because we want to focus on energy dissipation in the ambient ICM, we assume that dissipation occurs only in the regions surrounding the buoyant gas. To this end we impose a condition that switches on viscous effects provided that the fraction of the injected gas in a given cell is smaller than 10^{-3} . The gas obeys a polytropic equation of state with an adiabatic index of $\gamma = 5/3$. Unlike in Paper I we do not assume that the active regions are initially underdense and overheated.

3. RESULTS

3.1. Morphology of X-ray Emission and Dissipation

The top row in Figure 1 shows X-ray maps of the heated cluster. The panels show five different epochs from earliest on the left to the latest on the right. We assumed that the main contributor to X-ray emissivity is free-free emission. The maps correspond to emission integrated in the energy band $E \in (2 - 10) \text{ keV}$. The axis of injection is located in the plane of the sky. The emissivity contrast between the injected material and the surrounding medium is strongest at the center. As the bubbles rise buoyantly in the cluster atmosphere, the contrast diminishes and so does the probability of detecting the bubbles.

The middle row in Figure 1 presents unsharp-masked X-ray images corresponding to the images on the top row. These images were generated by smoothing the original X-ray map and subtracting the original X-ray map. Smoothing was done by convolving the original image with a Gaussian filter centered on a given point. The full width at half maximum of the adopted Gaussian distribution was $\sim 6 \text{ kpc}$. It is evident from this figure that ripples outside bubble locations are visible. As discussed below, these perturbations are the sound waves/weak shocks. Note also that the interfaces between the bubble location and the ICM are clearly present in these maps. This means that the ripples in the Perseus cluster can be due to a combination of sound waves, weak shocks and interfaces between the ICM and fossil bubbles.

The bottom row in Figure 1 shows the viscous dissipation rate ($\text{erg s}^{-1} \text{ g}^{-1}$) associated with the dispersing waves seen in the middle row. These maps show cross-sections through the cluster center that are perpendicular to the line of sight.

3.2. Spatial Distribution of Heating and Total Dissipation

In Figure 2 we show the ratio of the viscous heating rate to the radiative cooling rate as a function of time for a range of radii. More distant regions are heated at later times and hence the curves corresponding to these regions rise at later times. It is interesting to note that the heating-to-cooling ratio is of order unity even for more distant regions close to the cooling radius. Thus, heating is well distributed spatially, even though the bubbles occupy a smaller volume than the waves. Note that the curves exhibit a clear periodic behavior which is due to the intermittency of the central source. We also note that this figure is similar to Fig. 2 in Paper I, thus confirming that one of the main conclusions of their paper holds in three-dimensional geometry.

Figure 3 shows the ratio of viscous heating to radiative cooling rate as a function of distance from the cluster center for equally-spaced time intervals of $\Delta t = 10^7$ yr until 2×10^8 yr. As time increases the curves start to decline at progressively larger radii. From this figure one can also deduce the characteristic speed of the wave pattern (see below) and compare it with analytical estimates.

Figure 4 shows the ratio of the volume-integrated heating rate to the volume-integrated cooling rate as a function of time. Note that this ratio is of order unity. Therefore, this heating mechanism has the potential for significantly affecting the rate at which the gas loses its internal energy or perhaps even offsetting radiative cooling altogether.

We stress that the actual value of the ratio of heating to cooling (Figs. 2–4) depends on the parameters adopted in the model. However, fine tuning may not be necessary as already argued by Paper I.

Additional heating may result from damping of large scale motions caused by entrainment and lifting of the gas surrounding the bubbles. This is the general mechanism proposed by Begelman (2001) and Ruszkowski & Begelman (2002) in their discussion of “effervescent heating”. The widespread spatial distribution of heat in this mechanism can be achieved when the buoyant bubbles rise in the ICM perturbed by preceding bubbles. That is, subsequent bubbles find lower resistance to move in all directions once they encounter underdense regions “drilled” by earlier bubbles. Moreover, when the bubbles move a substantial distance from the cluster center, the lateral spreading is further enhanced as the bubble entropy becomes comparable to the entropy of the ambient medium. Spatial spreading of heat could also be facilitated if the jet (or other form of outflows) precesses or if the black hole in the center of the AGN adjusts in response to a change in the orientation of the accretion disk. This could be triggered by a merger with a substructure clump in the cluster or by the oscillatory motion of the AGN around the cluster center of gravity (see e.g. Johnstone et al. 2002).

3.3. Energy Transfer Between the Bubbles and the ICM

In Figure 5 we present the cumulative injected energy E_{inj} (solid curve), energy contained in the rising bubbles E_{bubb} (dashed) and the energy transferred to the ICM ($E_{\text{tran}} \equiv E_{\text{inj}} - E_{\text{bubb}}$; dotted). The bubble energy E_{bubb} is defined as

$$E_{\text{bubb}} \equiv \int_{\text{bubb}} [e_{\text{pot}}(t) + e_{\text{int}}(t) + e_{\text{kin}}(t)] \rho dV$$

$$- [e_{\text{pot}}(0) + e_{\text{int}}(0)] \rho_0(2V_0), \quad (1)$$

where e_{pot} , e_{kin} and e_{int} are the gravitational potential, specific kinetic energy density and specific internal energy density, respectively. The $2V_0$ factor is the total volume of the initial injection regions. The integration is performed over the volume of the bubbles. The bubble energy increases during outbursts and then decreases during dormant phases. The decrease of the energy in the bubbles with time can be attributed to two factors: (i) energy is transferred to the ambient medium via PdV work and because the rising bubble experiences drag from the surrounding gas and (ii) mixing of the bubble and the ICM gas. Recall that the bubble is defined as the region where the fraction of the injected gas is greater than 10^{-3} (this region overlaps exactly with the low density bubble region). This assures that essentially no energy injected into the bubble is omitted in the calculation of the bubble energy. The contribution to the bubble energy from the gravitational potential is relatively small. Since mixing occurs without a significant change in pressure and the bubble internal energy is proportional to pressure, the change in bubble energy comes mostly from the PdV work done by the bubble against its surroundings and the drag on the bubble from the ambient ICM.

The fraction of the AGN energy that is transferred to the surrounding ICM is plotted in Figure 6 (solid curve). The ratio of viscously dissipated energy to the energy injected by the AGN is plotted as the bottom (dashed) curve in Figure 6. This figure indicates that approximately 35 per cent of the energy injected by the AGN remains in the buoyant bubbles while the rest is transferred to the surrounding ICM and that about 25 per cent of the injected energy ends up heating the ambient ICM viscously. We point out that not all of the energy that is transferred to the ICM is converted to heat. It is viscous dissipation that is responsible for heating the gas. The fraction of the injected energy that is transferred to the ambient ICM agrees qualitatively with simple analytical estimates presented in Paper I. For the adopted adiabatic index and assuming pressure equilibrium between the bubble and the ICM about 40% of the input energy can be transferred to the ambient gas. Because the cavities are mildly overpressured, the fraction of the input power transferred to the ICM in the actual simulation is a little larger.

3.4. Wave decay

From Figure 3 one can deduce the characteristic speed of the wave pattern which we found to have a Mach number of ~ 1.3 . Thus, the waves can be interpreted as strong sound waves or weak shocks. In the weakly nonlinear regime, the speed of the wave is $c_s(1 + [(\gamma + 1)/2]\alpha)$, where c_s is the sound speed and $\alpha \sim \delta\rho/\rho$ is the normalized wave density amplitude (Stein & Schwartz 1972, Mihalas & Mihalas 1984). For the typical amplitudes seen in the simulation, the wave speed of Mach 1.3 is consistent with these estimates.

In Figure 7 we show the energy flux of the decaying wave corresponding to the initial outburst. The simulation results are denoted by filled squares connected by a solid line. Also shown for reference is the decay profile corresponding to $\sim r^{-2}$. All curves have arbitrary units. The

period-averaged wave energy per unit time that is streaming through a surface S in a direction perpendicular to this surface is $L_w \sim (\delta P)^2 S / (\rho v_w)$, where v_w is the wave speed. In the absence of any dissipation, the energy flux should scale as $\sim r^{-2}$. However, the slope of the energy flux in our simulations is steeper. This means that viscous dissipation plays an important role in tapping the wave energy.

The characteristic dissipation length l can be estimated from $l \sim 70\lambda_{10}^2 n_{0.02} T_4^{-2}$ kpc, where $\lambda = 10\lambda_{10}$ kpc, $n = 0.02n_{0.02}$ cm $^{-3}$ and $T = 4T_4$ keV (Fabian et al. 2003a, cf. Landau and Lifshitz 1975). The dissipation length can also be estimated from $l \sim [\partial \ln(\rho\alpha^2) / \partial r + 2/r]^{-1}$, where $\alpha \equiv \delta\rho/\rho$ is the normalized density amplitude of the wave and can be directly derived from the simulation results. At $r \sim 55$ kpc, the dissipation length is of order 40 kpc, which is qualitatively consistent with the above simple analytical estimates.

3.5. Caveats

We stress that our use of the Spitzer viscosity is meant to be illustrative and may not accurately represent the momentum transport in the magnetized intracluster medium. For one thing, magnetic shear stresses are likely to dominate over molecular viscosity in the transport of bulk momentum. This could either enhance or suppress the dissipation of sound waves, and will almost certainly make the dependence of stress on the velocity field more complicated. For another, in this macroscopic form of momentum transport the rate of dissipation (due to reconnection) would be nonlocally related to the stress tensor. Treatment of these effects will require high-resolution magnetohydrodynamical simulations. Moreover, magnetic fields could introduce effects similar to bulk viscosity, as a result of plasma microinstabilities. In our simulations we neglected bulk viscosity since it vanishes for an ideal gas. We note that bulk viscosity, if present, could dissipate waves even more efficiently. Finally, we have neglected the effects of thermal conduction, which (assuming Spitzer conductivity) could damp the sound waves more quickly than Spitzer viscosity (since the conductive dissipation rate exceeds the viscous one by a factor ~ 10 under the simplified assumption that waves are linear and that the gas has constant density and pressure and gravity can be neglected; see Landau and Lifshitz 1975). We point out that, as long as the waves are linear, the nature of the wave decay due to Spitzer viscosity or Spitzer conductivity is the same, i.e., the only change is the constant damping coefficient. Note that the waves considered here are either linear (sound waves) or weakly non-linear (weak shocks) and characterized by a relatively small Mach number. Since conductivity is expected to be suppressed by magnetic fields, a realistic assessment of whether conduction enhances the damping rate of sound waves is beyond the scope of this investigation. If the dissipation rate significantly exceeds the Spitzer value, then the sound waves will be damped more efficiently and only the gas close to the bubbles will be heated efficiently.

We now argue that the choice of boundary conditions has negligible effects on our results. First of all, the issue of reflection has no effect at all on our results presented in Figures 4, 5, 6 and 7. This is because the waves had

no time to reach the boundary for the times considered in these figures.

The waves reach the boundary approximately at time $\sim 6 \times 10^7$ yr. However, there is no clear rapid rise in the dissipation rate for the times before and after this time. No such jump is seen in Figure 2 (e.g., for the curves that correspond to outer shells in the cluster, where the reflection effects should be seen immediately) or in Figure 4, which shows the total dissipation rate. Had the reflection been important, such a jump would have been clearly visible.

In the last row of Figure 1, 2nd (earlier time) and 3rd (later time) columns, shows the dissipation wave in the process of crossing the boundary. No reflection is seen in either 2nd or 3rd column figure. Also, the wave fronts in the corners propagate across the boundary without any obvious signs of strong reflection.

It is known that for supersonic fluctuations the outflow boundary conditions are exact and no reflections are expected. The fact that our waves are strong sound waves or weak shocks traveling at mildly supersonic velocities helps to minimize reflections.

In principle, the outflow boundary conditions can be made arbitrarily close to the exact ones if the simulation resolution is sufficiently high. That is, the error made by replacing the ghost zone solution based on some exact method by the value copied from the last active zone (outflow boundary condition) tends to zero as the resolution increases. Similarly, when the perturbations in question are smoother, the outflow boundary conditions give a more accurate answer because the waves are better resolved. We note that the effect of dissipation is to disperse the waves and make them more easily resolvable. Moreover, the amplitude of the waves decays faster in 3D than in 2D. Thus, in 3D the effects of reflection are reduced.

The outflow boundary conditions are exact for a wave traveling along the boundary. Therefore, the degree to which a wave is reflected decreases for waves moving at an angle to the boundary.

4. SUMMARY

To summarize, we have analyzed the energy deposition in the cluster due to rising bubbles, sound waves and weak shocks. This was motivated by the recent discovery of such waves in the Perseus cluster by Fabian et al. (2003a) and in the Virgo cluster by Forman et al. (2004). We found that the dissipated energy may be comparable to the cooling rate, thereby significantly affecting the cooling flow or even quenching it altogether. We showed that about 65 per cent of the energy injected by the central source can be transferred to the ICM. Approximately 25 per cent of the energy injected by the AGN can be converted to heat, assuming Spitzer viscosity. We discussed the wave decay rates and showed that a significant fraction of wave energy is deposited within the cooling radius. The computed decay rates are consistent with linear theory estimates of the damping length. The damped sound waves or weak shocks are still detectable in unsharp-masked X-ray images. Old bubbles become increasingly difficult to detect in the X-ray maps as the contrast between the rising bubbles and the surrounding gas diminishes. However, apart from sound waves and weak shocks in unsharp-masked X-

ray maps, the interfaces between the intracluster medium and old bubbles are also clearly visible. This opens up the possibility of detecting fossil bubbles that are difficult to detect in radio emission.

MR thanks Daniel Proga for discussions. Support for this work was provided by National Science Foundation grant AST-0307502 and the National Aeronautics and Space Administration through *Chandra* Fellowship Award Number PF3-40029 issued by the Chandra X-ray Observatory Center, which is operated by the Smithsonian

Astrophysical Observatory for and on behalf of the National Aeronautics and Space Administration under contract NAS8-39073. MB acknowledges support by DFG contract BR2026/2 and thanks JILA, University of Colorado at Boulder for their hospitality. The software used in this work was in part developed by the DOE-supported ASCI/Alliance Center for Astrophysical Thermonuclear Flashes at the University of Chicago. Preliminary computations were performed on JILA Keck cluster sponsored by the Keck Foundation.

REFERENCES

Batchelor, G.K. 1967, *An Introduction to Fluid Dynamics*, Cambridge University Press, Cambridge

Blanton, E.L., Sarazin, C.L., McNamara, B.R., & Wise, M.W. 2001, *ApJ*, 558, 15

Braginskii, S.L. 1958, *Sov. Phys. JETP*, 6, 358

Brightenti, F., & Mathews, W.G. 2003, *ApJ*, 587, 580

Brüggen, M. 2003, *ApJ*, 592, 839

Brüggen, M., & Kaiser, C.R. 2002, *Nature*, 418, 301

Brüggen, M., Kaiser, C.R., Churazov, E., & Enßlin 2002, *MNRAS*, 331, 545

Churazov, E., Brüggen, M., Kaiser, C.R., Böhringer, H., & Forman, B. 2001, *ApJ*, 554, 261

Churazov, Sunyaev, Forman, & Böhringer 2002, *MNRAS*, 332, 729

Fabian, A.C. 1994, *ARA&A*, 32, 277

Fabian, A.C., Sanders, J.S., Allen, S.W., Crawford, C.S., Iwasawa, K., Johnstone, R.M., Schmidt, R.W., & Taylor, G.B. 2003a, *MNRAS*, 344, 43

Fabian, A.C., Sanders, J.S., Crawford, C.S., Conselice, C.J., Gallagher, J.S., & Wyse, R.F.G. 2003b, *MNRAS*, 344, 48

Forman, W. et al. 2004, *ApJ*, submitted, astro-ph/0312576

Hansen, H.H. & Stadel, J. 2003, *ApJ*, 595, 37

Johnstone, R.M., Allen, S.W., Fabian, A.C., & Sanders, J.S. 2002, *MNRAS*, 336, 299

Landau, L.D & Lifshitz, E.M. 1975, *Fluid Mechanics*, Pergamon Press

McNamara, B.R., et al. 2000, *ApJ*, 534, 135

Mihalas, D., & Mihalas, B.W. 1984, *Foundations of Radiation Hydrodynamics* (New York: Oxford Univ. Press)

Navarro, J., Frenk, C., & White, S. 1995, *MNRAS*, 275, 720

Navarro, J., Frenk, C., & White, S. 1997, *ApJ*, 490, 493

Peterson, J.R., Puerls, F.B.S., Kaastra, J.S., et al. 2001, *A&A*, 365, 104

Peterson, J.R., Kahn, S.M., Puerls, F.B.S., Kaastra, J.S., et al. 2003, *ApJ*, 590, 207

Quilis, V., Bower, R., & Balogh, M.L. 2001, *MNRAS*, 328, 1091

Reynolds, C.S. et al. 2004, submitted to *MNRAS*, astro-ph/0402632

Ruszkowski, M., & Begelman, M.C. 2002, *ApJ*, 581, 223

Ruszkowski, M., Brüggen, M., & Begelman, M.C., 2004, *ApJ*, in press, astro-ph/0310760, Paper I

Shu, F.H., 1992, *The Physics of Astrophysics*, Vol.2, *Gas Dynamics*, University Science Books, Sausalito, CA

Stein, R.F., & Schwartz, R.A. 1972, *ApJ*, 177, 807

Sutherland, R.S., & Dopita, M.A. 1993, *ApJS*, 88, 253

Tamura, T., Kaastra, J.S., Peterson, J.R., Puerls, F., et al. 2001, *A&A*, 365, 87

Tozzi, P., & Norman, C. 2001, *ApJ*, 546, 63

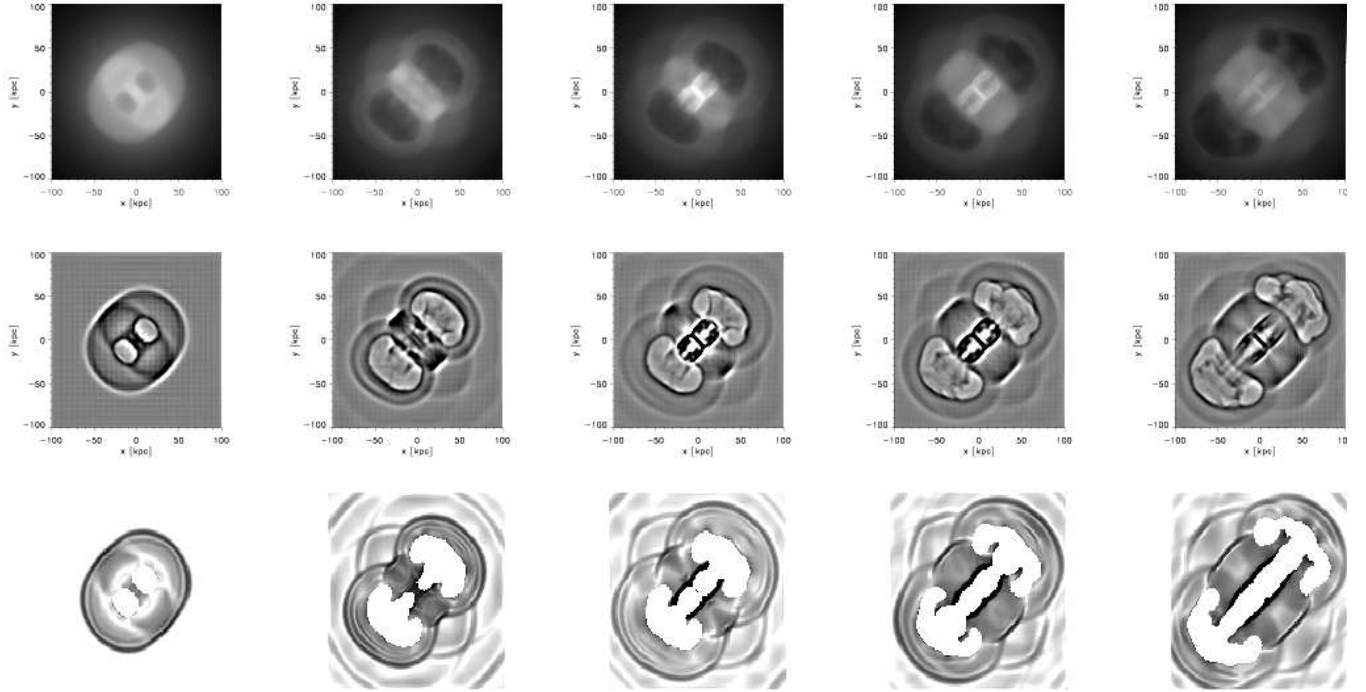


FIG. 1.— Top row shows the X-ray emissivity maps of the AGN-heated cluster. Snapshots correspond to 3.0×10^7 , 1.15×10^8 , 1.25×10^8 , 1.55×10^8 and 1.85×10^8 years, from left to right, respectively. Middle row shows X-ray unsharp masked maps corresponding to X-ray maps. Bottom row shows the map of the viscous dissipation pattern. Whereas the maps in the bottom row show cross-sections through the cluster center that are perpendicular to the line of sight, the first two rows correspond to projections onto the plane of the sky.

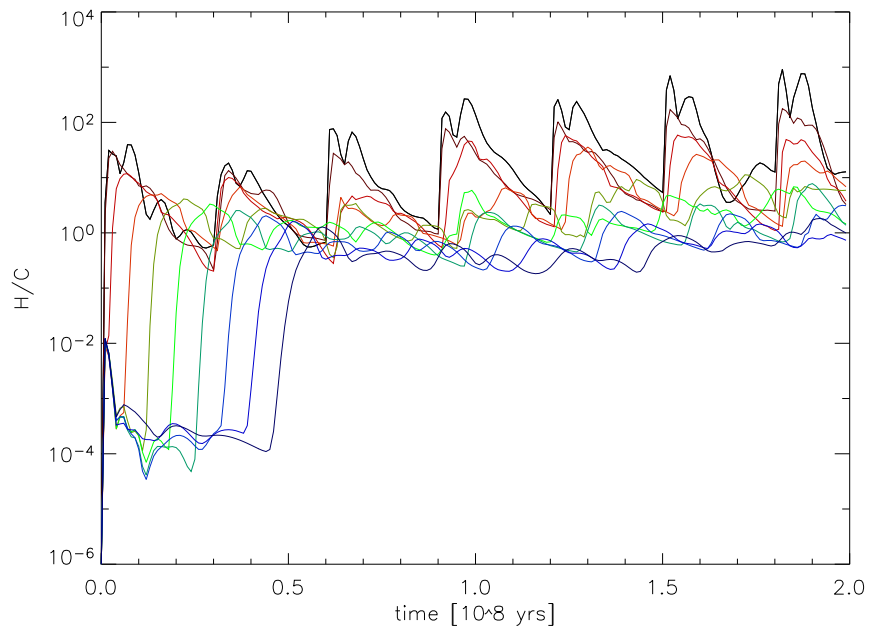


FIG. 2.— The ratio of viscous heating to radiative cooling rate as a function of time for a number of concentric shells around the cluster center. The curves that start rising at later times correspond to shells located further away from the center. The heating-to-cooling ratio was calculated in ten shells starting from the first shell at 5 kpc and the remaining shells located in increments of 10 kpc away from the cluster center. Note that the heating rate is comparable to the cooling rate.

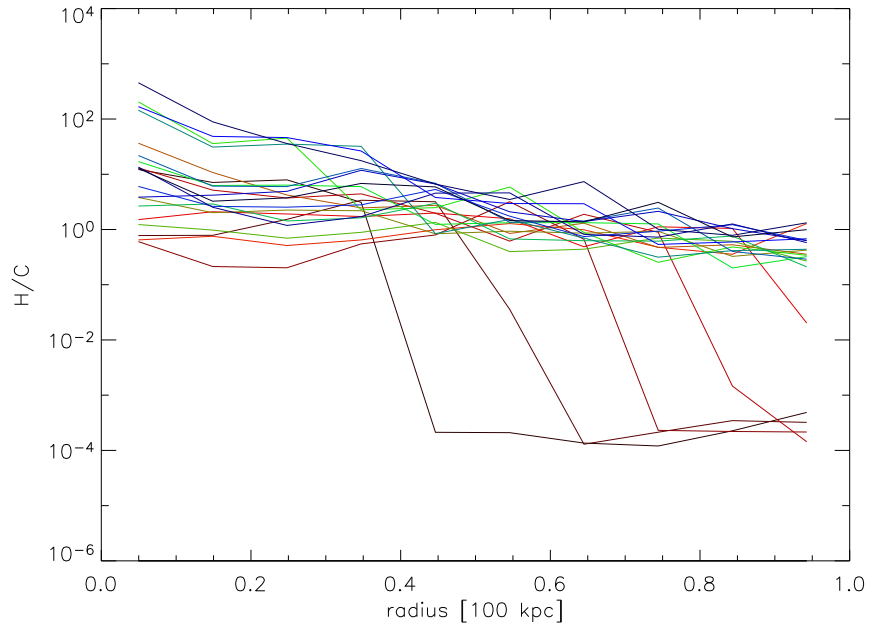


FIG. 3.— The ratio of viscous heating to radiative cooling rate as a function of distance from the cluster center for equally-spaced time intervals of $\Delta t = 10^7$ yr until 2×10^8 yr.

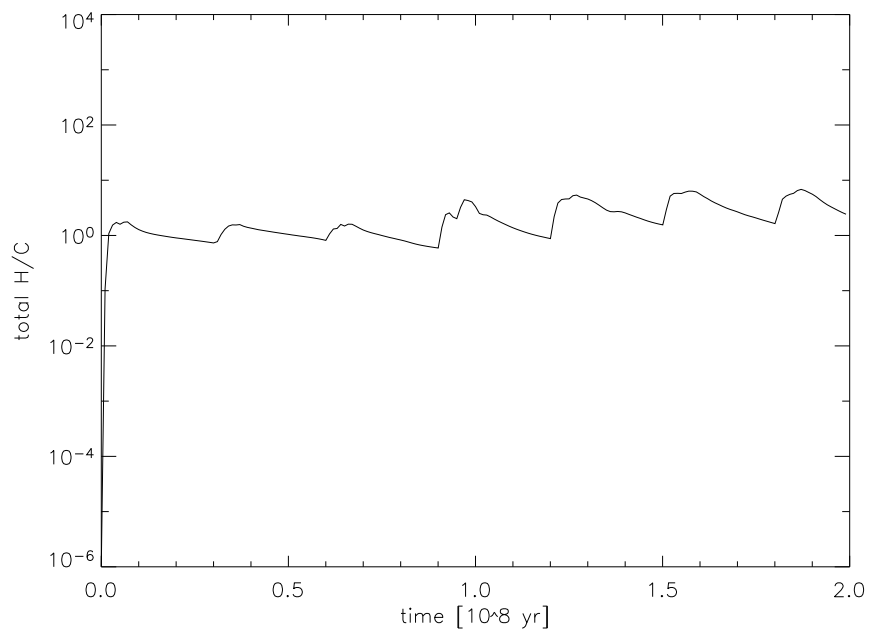


FIG. 4.— The ratio of volume-integrated heating rate (within 100 kpc from the center) to volume-integrated cooling rate as a function of time.

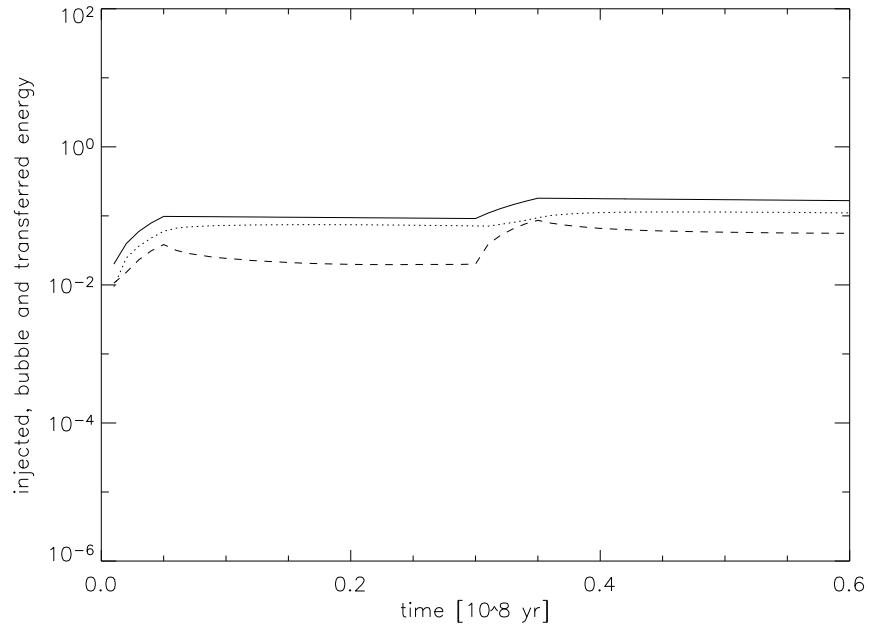


FIG. 5.— The cumulative injected energy E_{inj} (solid curve), bubble energy E_{bubb} (dashed curve) and energy transferred to the ambient ICM ($\equiv E_{\text{inj}} - E_{\text{bubb}}$; dotted curve) as a function of time. All plots are in arbitrary units. We only plot data until 60 Myr as for later times the waves start to escape the computational box.

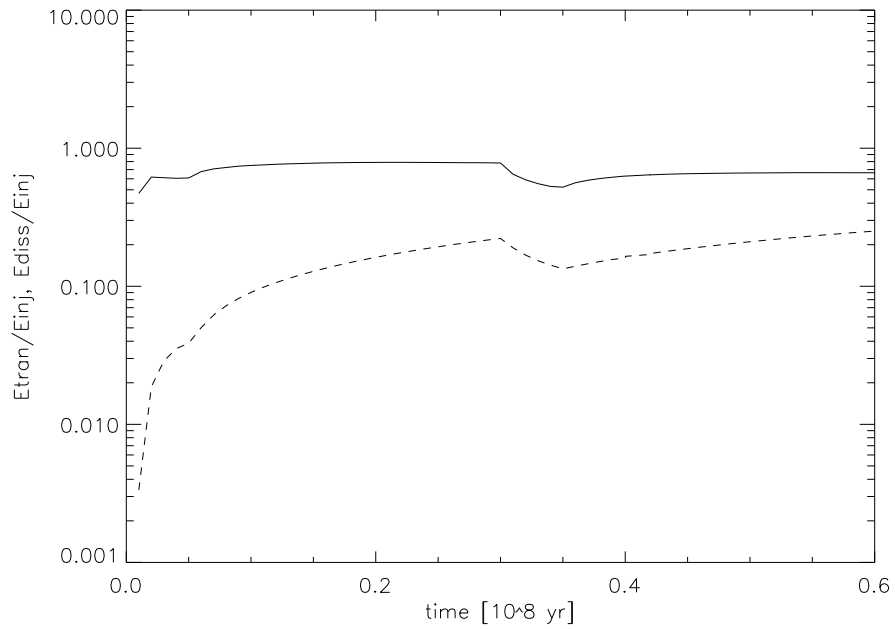


FIG. 6.— The ratio of cumulative transferred energy to the cumulative injected energy (top curve) and the ratio of the cumulative viscously dissipated energy to the cumulative injected energy as a function of time. We only plot data until 60 Myr as for later times the waves start to escape the computational box.

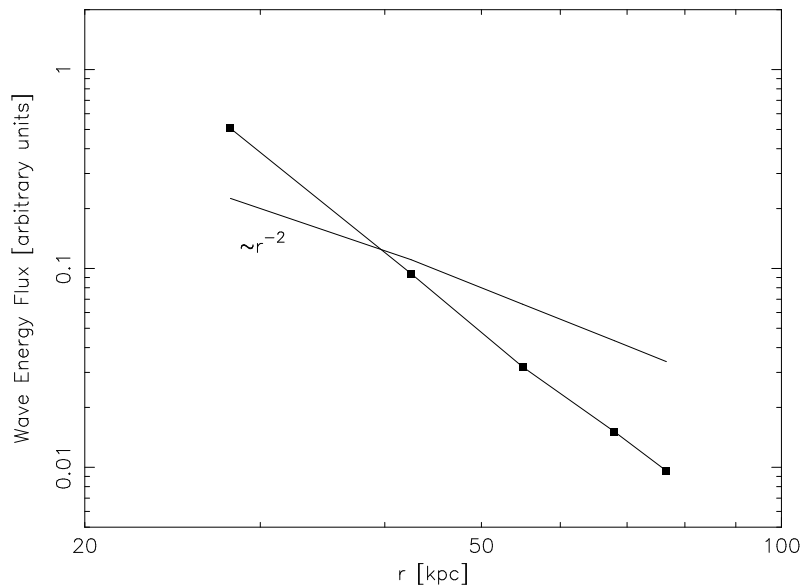


FIG. 7.— The wave energy flux as a function of the distance from the cluster center. The $\sim r^{-2}$ decay profile is shown for comparison. All quantities are in arbitrary units.